Letter

High Performance Bubble Manipulation on Ferrofluid-Infused Laser-Ablated Microstructured Surfaces

Suwan Zhu, Yucheng Bian, Tao Wu, Chao Chen, Yunlong Jiao, Zhiwu Jiang, Zhouchen Huang, Erqiang Li, Jiawen Li,* Jiaru Chu, Yanlei Hu,* Dong Wu,* and Lei Jiang

Cite This: *Nano Lett.* 2020, 20, 5513−5521

Read Online

ACCESS | Metrics & More | Article Recommendations | Supporting Information

ABSTRACT: Manipulation of gas bubbles in an aqueous ambient environment is fundamental to both academic research and industrial settings. Present bubble manipulation strategies mainly rely on buoyancy or Laplace gradient forces arising from the sophisticated terrain of substrates. However, these strategies suffer from limited manipulation flexibility such as slow horizontal motion and unidirectional transport. In this paper, a high performance manipulation strategy for gas bubbles is proposed by utilizing ferrofluid-infused laser-ablated microstructured surfaces (FLAMS). A typical gas bubble (<2 μL) can be accelerated at >150 mm/s^2 and reach an ultrafast velocity over 25 mm/s on horizontal FLAMS. In addition, diverse powerful manipulation capabilities are demonstrated including antibuoyancy motion, "freestyle writing", bubble programmable coalescence, three-dimensional (3-D) controllable motion and high towing capacity of steering macroscopic object (>500 own mass) on the air−water interface. This strategy shows terrain compatibility, programmable design, and fast response, which will find potential applications in water treatment, electrochemistry, and so on.

KEYWORDS: *gas bubbles, ferrofluid, femtosecond laser, slippery surfaces, bubble manipulation*
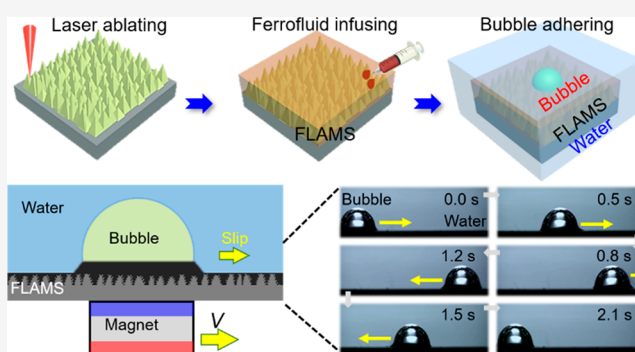
Gas bubbles are ubiquitous in nature and organisms but remain challenging to manipulate toward arbitrary direction at will. Controllable movement of gas bubbles in aqueous condition is fundamental to both academic research and industrial settings, such as water treatment, electrochemistry, mass delivery, and mineral floatation.[1−4] For instance, humpback whales hunt fishes by producing numerous tiny gas bubbles around them.[5] Detachment of gas bubbles on a heated surface can significantly boost the efficiency of boiling heat transfer.[6−9] To date, existing strategies for manipulating gas bubbles mainly rely on the assistance of buoyancy force or the cooperation of wetting driving force and Laplace pressure stemming from substrate's morphology.[10−16] Nevertheless, these manipulation strategies are still plagued with problems that restrict their practical applications: (1) Most designs suffer from the shortage of unidirectional bubble transport, which greatly hindered its practical application in real-time bubble control (e.g., pinning/sliding or active guidance during bubble motion). For buoyancy-assisted strategy, the dominant buoyancy force imposes great restriction on motion control except floating up, and thus the bubbles could only be driven on tilted surfaces, while for wetting/Laplace-gradient-assisted strategy, the bubble could only transport along the direction of the gradient force field. (2) On a planar platform, antibuoyancy bubble motion remains a great challenge. For wetting/Laplace-
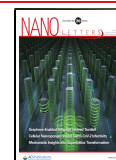
gradient-assisted strategy, the key driving forces are weak and restrained by the substrate's sophisticated geography (e.g., tapered or helical shapes). Therefore, current studies are far from the practical requirement of rapid bubble movement toward arbitrary direction at will.[17,18]

In nature, the unique surface of the *Nepenthes* pitcher plant with an aqueous lubricant layer endows itself with insect-capturing capability due to its excellent sliding properties. Inspired by this intriguing plant, lubricant-infused surfaces have been proposed to repel a wide range of materials (e.g., liquid, ice, organism) with low contact angle hysteresis (<5°) at high pressures (up to ~680 atm).[19−22] Recently, Aizenberg and co-workers developed a state-of-the-art hierarchical magnetism-responsive composite surface by infiltrating ferrofluid into a microstructured matrix.[23] By virtue of magnetic force gradient, the motion of magnetic nanoparticles suspended in the ferrofluid will lead to macroscopic motion of the ferrofluid within the microstructured surface. Con-
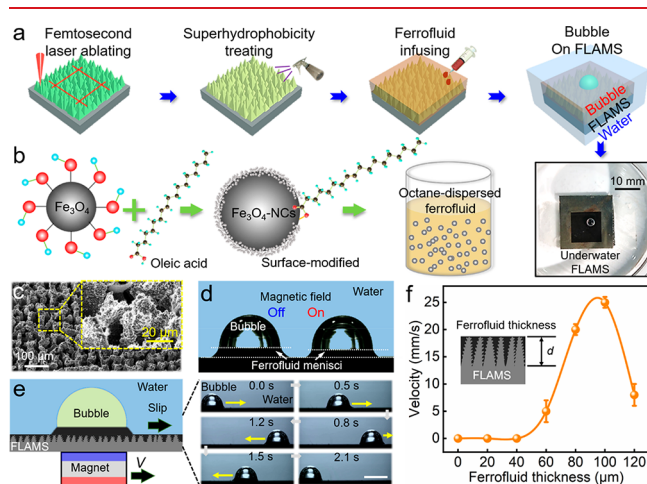
sequently, the magnetism-responsive composite surfaces offer paradigms for manipulation of a droplet cluster with unique characteristics such as controlled formation, switchability, and directional adhesion. Inspired by the excellent droplet manipulation performance on the ferrofluid-impregnated surface featuring extremely low hysteresis and high mobility in relatively low magnetic fields,[24] this kind of active surface is highly promising to solve the above-mentioned key issues of rapid bubble motion on a planar substrate toward an arbitrary direction.

Herein, we put forward a magnetism-responsive manipulation strategy with ultrafast transport toward arbitrary direction for underwater bubbles on FLAMS, which is constructed via the simple infusion of laser-ablated microstructured Ni−Ti alloy sheet with a smooth slippery ferrofluid in aqueous condition. By taking advantages of the aerophilic magnetism-responsive FLAMS surface, typical gas bubble (<2 μL) can be accelerated at over 150 mm/s^2 and reach an ultrafast velocity over 25 mm/s (equivalently 25 body-length/s). Moreover, diverse powerful manipulation capabilities are demonstrated, including antibuoyancy motion (up to 90° tilt angle), "freestyle writing", bubble programmable coalescence, three-dimensional (3-D) controllable motion, and high towing capacity of the steering macroscopic object (>500 own mass) on the air−water interface, which are otherwise difficult for conventional approaches suffering from unidirectional transport and slow horizontal motion. This study provides a powerful construction concept to design smart slippery surfaces for the flexible manipulation of gas bubbles.

First, the planar Ni−Ti alloy sheet was microstructured by femtosecond laser ablation (Figure 1a and Figure S1, Supporting Information). We chose this material because of its good chemical resistance and biocompatibility. The as-

prepared sample was then treated into superhydrophobicity with a water contact angle of ~154° (Figure S2, Supporting Information). Second, we infiltrated the superhydrophobic substrate a kind of ferrofluid containing Fe_3O_4 nanoparticles synthesized by coprecipitation method (Figure S3, Supporting Information),[25] to form the aerophilic FLAMS (Figure 1b) with a bubble contact angle of 75.3 ± 2.5° (Figure S2, Supporting Information). Surface morphology of the laser-ablated substrate was visualized through SEM images, showing the average distance of ~20 μm between two adjacent microbumps (Figure 1c). During the laser ablation process, the smooth surface of the Ni−Ti alloy was induced by a femtosecond laser spot to form the net-like micro/nanostructures under the combined effect of pulse laser shock compression and debris deposition. The depth of the groove structure on Ni−Ti substrate was measured to be ~60 μm (Figure S4, Supporting Information). The micro/nanostructured substrate features the excellent capability to lock in place the infused ferrofluid for FLAMS.[19] The maximum bubble load on FLAMS was measured to be 30 μL (Figure S5, Supporting Information).

The static configurations of a 20 μL bubble on FLAMS are shown in Figure 1d. A ferrofluid meniscus was formed around the bottom of the bubble. Once an external magnetic field was applied, the surrounding meniscus shrunk. The ferrofluid meniscus is crucial for bubble manipulation, as it bridges the mechanical interplay between the gas bubble and external magnetic force. Figure 1e shows the typical bubble slipping process on the FLAMS under magnetic actuation. Furthermore, the typical relation between ferrofluid thickness and bubble transport velocity was quantified (Figure 1f), suggesting that a maximum velocity of 25 mm/s appeared when the ferrofluid thickness d was ~100 μm, where d is defined as the distance between the upper surface of the ferrofluid and the bottom groove of the microstructured substrate. Unless otherwise specified, 100 μm thick ferrofluid was used throughout the experiments. On the basis of the one-step high-efficiency femtosecond laser fabrication without multistep chemical treatment and the subsequent environment pollution, a series of bubble motion behaviors on the FLAMS were investigated in the following section.

The bubble coalescence with ferrofluid and the formation of the rising ferrofluid meniscus were further investigated. Once the bubble touches the water−ferrofluid interface, it prefers to stay inside the octane phase to minimize the surface energy of the system. Depending on the static Newmann conditions at the triple-line,[26,27] the bubble will either pass fully through the water−ferrofluid interface, or get trapped at the interface through the interplay with the water−ferrofluid interfacial energy.[28] We employed a high-speed Video camera system to record the rapid dynamic process (Figure S6, Supporting Information). As shown in Figure 2a, the neck radius r grew rapidly with time after contact. Meanwhile, a yellow thin layer of ferrofluid can be observed to climb up along the bubble surface. The growth of the neck radius was characterized with a power law of $r \sim t^{1/2}$.[29] The viscosity can slow down this speed and leads to an exponent smaller than 0.5 by following $r/R_b \sim (t/\tau_{\Delta\sigma})^{0.44}$,[28] where R_b is bubble radius and $\tau_{\Delta\sigma} = \sqrt{\rho_w R_b^3 (2/\Delta\sigma)}$ is the capillary-inertial time scale based on water density and on the net interfacial tension $\Delta\sigma = \sigma_{aw} + \sigma_{ow} - \sigma_{ao}$ (σ_{aw}, σ_{ow}, and σ_{ao} represent the interfacial tensions of air−water, octane−water, and air−octane inter-
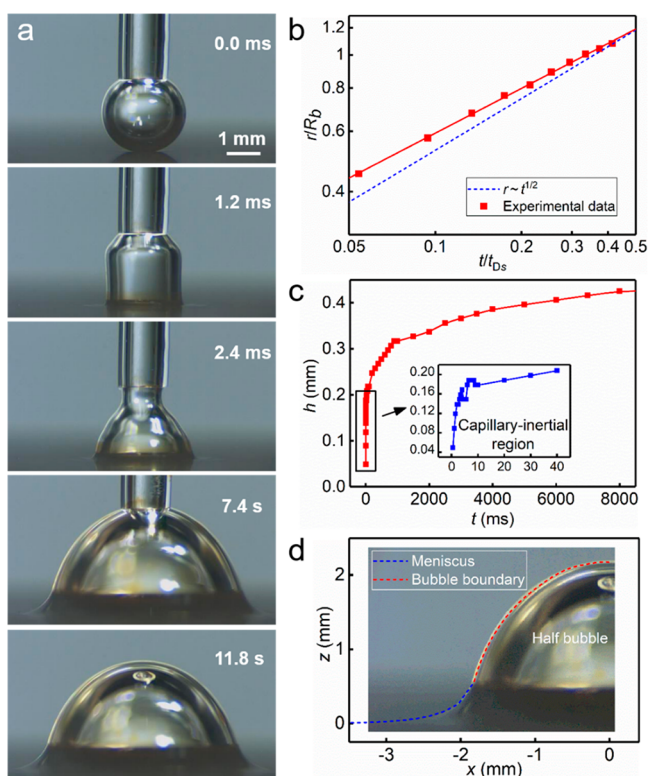

Figure 1. Design and fabrication of FLAMS for high performance bubble manipulation. (a) The NiTi alloy substrate is microstructured by laser ablation and then treated into superhydrophobicy. Subsequently, the superhydrophobic substrate is infused with ferrofluid. (b) Synthesis process of the ferrofluid is shown. (c) Surface morphology observed by SEM at different magnifications is shown. (d) Once a magnetic field is imposed on the bubble, the ferrofluid meniscus shrinks. (e) On the left is the schematic of a magnetism-actuated bubble slipping on FLAMS, and on the right are snapshots of bubble slipping process on FLAMS. The scale bar is 2 mm. (f) The typical relation between ferrofluid thickness and bubble transport velocity suggests that a maximum velocity of ~25 mm/s appeared as the ferrofluid thickness d was set to be ~100 μm.

Figure 2. Transient interaction process between bubble and underwater FLAMS. (a) Dynamic interaction between the bubble and FLAMS surface, including bubble coalescence with ferrofluid and formation of rising ferrofluid meniscus. (b) Scaling law of neck radius versus time during coalescence process of bubble and immiscible liquid−liquid interface. The blue dashed line shows the growth of the neck radius with the power-law $r \sim t^{1/2}$, and the solid red line represents the experimental fitting result. (c) Relation between rising height of meniscus and time. (d) Final shape and height of ferrofluid meniscus obtained by numerically solving the Young−Laplace equation using a corrected density of ferrofluid, as the double-colored curve depicts.

faces, respectively). Our experimental data predicted a similar exponent of 0.43, as shown in Figure 2b.

When a triple-line is formed between the bubble and the liquid interface, the imbalance of the three interfacial tension causes the motion of the contact line. Here the height of the bulk ferrofluid at the bottom of the bubble is important as it could affect the magnetic force, and its evolution with time is shown in Figure 2c. The final configuration and height of the water−ferrofluid interface are determined by the Young−Laplace equation[30]

$$\frac{d\theta}{ds} - \frac{\cos\theta}{r + R_b} = \frac{z}{a^2} \qquad (1)$$

where $a = \sqrt{\sigma_{ow}/\Delta\rho g}$ is the capillary length, z is the height of interface. However, in our experiments, the density of water is greater than the density of ferrofluids, the hydrostatic pressure difference for maintaining the shape of the interface is missing (Figure 1d). Consequently, we have to correct the density of the octane, which essentially correct the capillary length a. This correction allows us to numerically solve the Young−Laplace equation and obtain the final shape of the water−ferrofluid interface (Figure 2d). The octane density correction could be understood as we treat the adhesion between the substrate and

the ferrofluid layer as an equivalent gravitational force. The bubble volume in Figure 2 is 15 μL, it should be noted that the correction of octane density might be dependent on the bubble volume, but that is out of the scope of this study.

To quantify the bubble horizontal transport velocity, we used a remote fashion by organizing three permanent magnets into a cluster under an acrylic water vessel. The mean magnetic flux density was measured to be ∼180 mT at the bubble center from a distance of 4 mm above the cluster. The magnet cluster was mounted on a mobile platform from a homemade railway system equipped with a speed-adjustable DC motor (Figure S7, Supporting Information). The driving velocity V_d would be readily tuned by different bias voltages applied on the motor. Here, three driving velocities (∼5, ∼21, and ∼35 mm/s) were employed to investigate the bubble motion limit under magnetic actuation, including acceleration and terminal velocity.

The detailed response of bubbles in various volumes (2, 4, 6, 8, and 10 μL) is shown in Figure 3 (also see Video S1, Supporting Information), in which each bubble was actuated instantly on the FLAMS and eventually reached the same terminal velocity ∼5 mm/s as V_d. When the bubble volume increased, the corresponding acceleration decreased significantly due to the enlarged resistance. The maximum motion limit for bubbles under elevated V_d was subsequently explored. Experimental results show that a bubble ($\leq$4 μL) could be accelerated at >100 mm/s^2 (under V_d = 35 mm/s) and reached a maximum velocity $\geq$20 mm/s on the FLAMS (Figure 3b,c). Particularly, for a 2 μL bubble, the acceleration even exceeded 150 mm/s^2, followed by a terminal velocity >25 mm/s. Nevertheless, larger bubbles (>4 μL) exhibited difficulty in fast transport because of the larger resistance stemming from both the ferrofluid and ambient water, which is positively associated with elevated velocities. In addition, the increase of V_d gives rise to enlarged initial acceleration but decreased bubble moving distance (Figure 3d). For the extreme case when V_d reached 35 mm/s, a 2 μL bubble got pinned eventually on the FLAMS. It can be clearly seen that the moving distance of the bubbles became shorter when the driving velocity V_d increased to both 21 and 35 mm/s, the underlying mechanism was briefly discussed in Figure S8, Supporting Information. Note that the maximum sliding velocity for a typical bubble (2 μL) can reach up to 25 mm/s, which is approximately 83 times the velocity (0.3 mm/s) in recently reported photothermal actuation method.[31] Moreover, different from the simple bubble pinning/sliding behavior achieved by alternately applying/removing an external magnetic field on tilt slippery gel surfaces,[32] the ultrafast horizontal bubble motion could be easily realized on our FLAMS platform.

To compare the bubble motion efficiency, we define the dimensionless number V_{bl}, i.e., the traveling distance per second relative to the body-length (body-length/s). In this work, a typical gas bubble (<2 μL) could reach up to a horizontal V_{bl} of 25, which exceeds the maximum burst speed record (V_{bl} = 21.1) for billfishes considered to be among the fastest swimmers in the oceans (Figure S9, Supporting Information).[33] Although higher transport velocities of the gas bubble have been reported on slippery and superhydrophobic cones,[13,15] the bubble transport is limited to unidirectional motion and is solely subject to the tailor-made topography of the substrate. In contrast, our manipulation
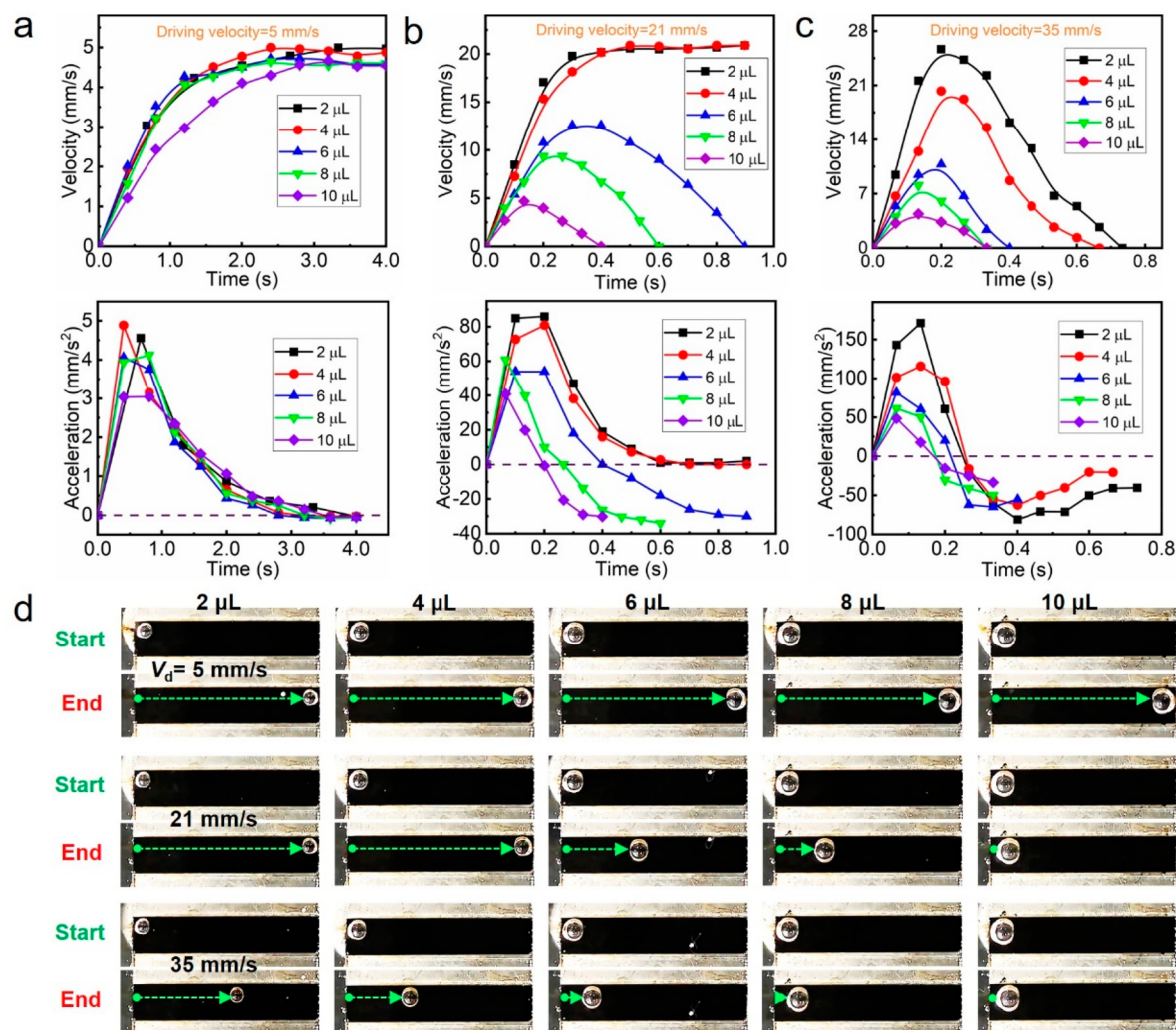
Figure 3. Ultrafast bubble transport process on horizontal FLAMS in diverse volumes. (a) All the bubbles can be accelerated and eventually reach the same terminal velocity of ~5 mm/s as the driving velocity V_d. (b) A bubble (≤4 μL) can be accelerated over 80 mm/s^2 and reach terminal velocity 21 mm/s. (c) When V_d is set to 35 mm/s, a bubble (≤4 μL) can be accelerated over 100 mm/s^2. For a 2 μL bubble, the acceleration exceeds 150 mm/s^2. (d) Snapshots of magnetism-actuated bubbles slipping process under various V_d are shown. The green dotted line connecting the left edge of the substrate and the bubble represents the total bubble displacement.

approach could readily achieve both arbitrary direction and rapid motion.

Our manipulation strategy exhibits not only the ultrafast transport capability but also the free directivity of bubble motion. This allows the bubbles to perform diverse complex actions, which unfolds new possibilities to overcome existing shortages from recently reported strategies. Figure 4a shows the consecutive snapshots of "freestyle writing" for a magnetism-actuated bubble on a horizontal FLAMS. The letter "U" was "written" within ~7.5 s, exhibiting free directivity with fast response (Video S2, Supporting Information). Moreover, by virtue of the manipulation flexibility, intriguing behavior of bubble programmable coalescence is also performed. As depicted in Figure 4b, the central bubble in the "bubble-matrix" was steered toward the six o'clock position and then slipped clockwise in succession, finally coalescing into a larger bubble within ~18.3 s (Video S3, Supporting Information).

Generally, antibuoyancy bubble motion is challenging because the dominant force, i.e., the buoyant force under water, imposes great restriction on bubble motion except

floating up. In our experiment we demonstrated the antibuoyancy motion capability of bubbles slipping downward along the FLAMS at different tilt angles (Figure 4c and Video S4, Supporting Information). At the maximum tilt angle of 90°, the bubble was capable of quickly slipping downward along the 20 mm long FLAMS track at t = 5.5 s. This powerful capability of antibuoyancy motion, i.e., slipping vertically downward, has performed well beyond our recently reported metric of 10° in antibuoyancy bubble motion.[31] The displacement versus time for antibuoyancy motion is shown in Figure 4d. With the increase of tilt angle, the average speed of the bubbles declined significantly during the antibuoyancy motion (magnetic field on) and then increased in the floating up motion from bottom to top (magnetic field off) due to the enlarged component force of buoyancy along the track.

The force analysis during the antibuoyancy process was further discussed (Figure 4e). There are five external forces acting on the bubble. The driving force of bubble motion is the component of the magnetic force, which is calculated as $F_{driving}$ = $F_{magnetic} \cdot \cos \alpha$ (where α is the included angle between magnetic force and the substrate, $\alpha > 0$) along the slipping
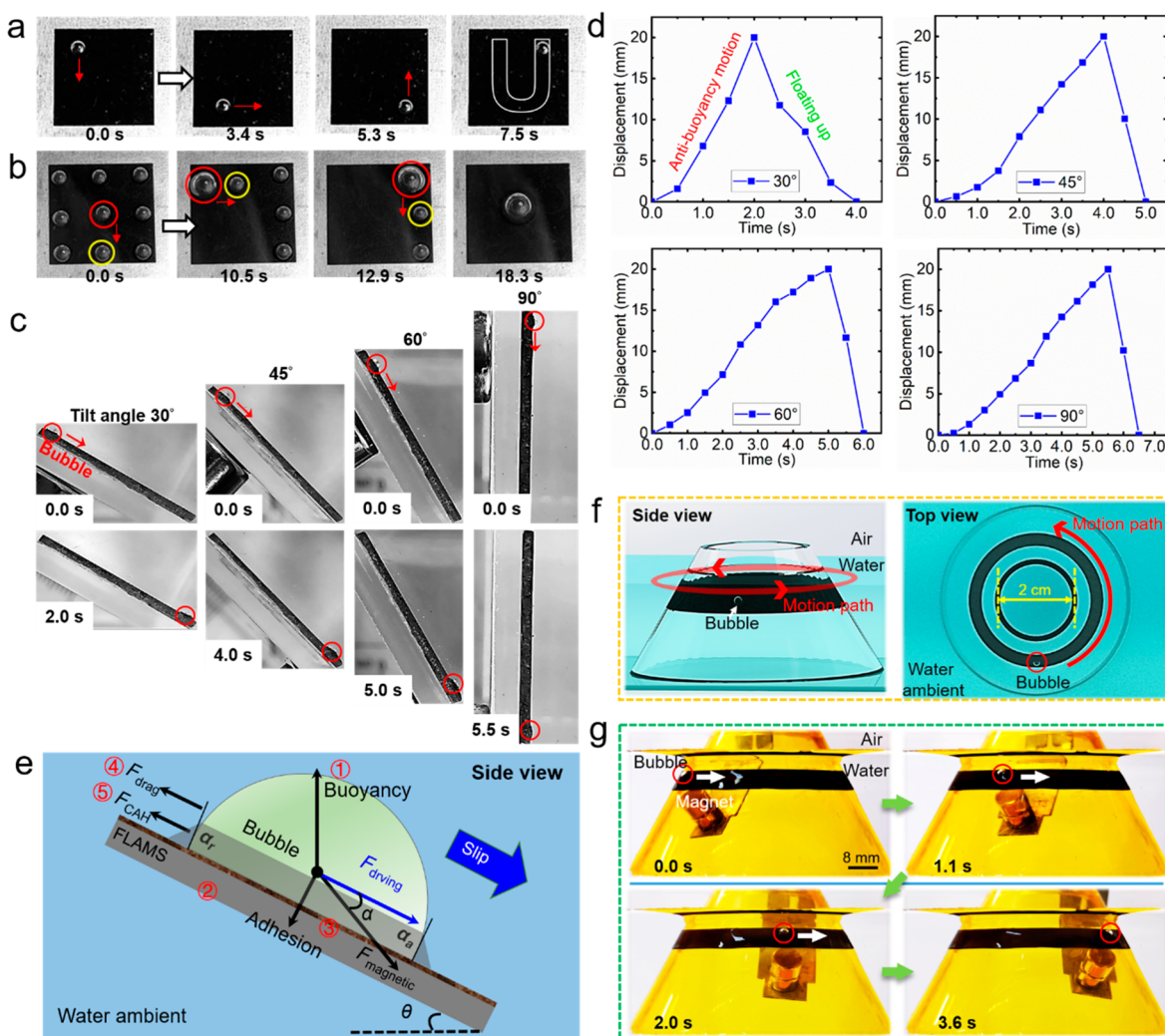
Figure 4. Complex actions of gas bubbles on planar and 3-D FLAMS. (a) Demonstration of "Freestyle writing" using a bubble on FLAMS. (b) Nine-bubble "matrix" coalescing sequentially into a larger bubble. (c) Antibuoyancy motion of bubbles along the FLAMS track at diverse tilt angles (30°, 45°, 60°, and 90°). (d) Displacement versus time during antibuoyancy and free-rise processes on the FLAMS track. (e) Force analysis of the antibuoyancy slipping process. (f) and (g) Controllable 3-D circular motion of a bubble on the external surface of a truncated cone.

direction. The total resistance in the opposite direction to the driving force consists of the component of buoyancy force F_b^* = $\rho \cdot V \cdot g \cdot \sin \theta$ (ρ, V, g and θ are water density, bubble volume, gravitational acceleration, and tilt angle of the substrate, respectively), contact angle hysteresis (CAH) of the bubble $F_{CAH} \approx \gamma \cdot L \cdot (\cos \theta_r - \cos \theta_a)$ (where γ, L, θ_a, and θ_r are the surface tension of ambient fluid, bubble's character length, and advancing/receding angle of bubble, respectively),[34] and fluid drag $F_{drag} \approx v^k$ (where k and v are the positive coeffcient and bubble velocity, respectively).[35] The adhesion force from the ferrofluid meniscus is balanced with the component of buoyancy force perpendicular to the slip direction. For a definite bubble, the critical slipping angle is solely determined by the magnitude of $F_{magnetic}$. In other words, a FLAMS-attached bubble can be steered at any tilt angle ($\leq 90°$) as long as $F_{magnetic} > (F_b^* + F_{CAH})/\cos \alpha$.

In addition to planar complex actions, our manipulation strategy is also generic for 3-D controllable bubble motion, as most of the recently reported bubble manipulation methods become invalid because of their rigid platform or slow antibuoyancy motion on curved surfaces. Figure 4 exhibits the controllable circular motion of a gas bubble on the surface

of a truncated cone. A hollow polypropylene funnel, on which an aluminum FLAMS loop (thickness 100 μm, width 5 mm) was fabricated and attached to its external surface, was partially immersed into a water tank (Figure 4f). Relying on the moving magnet cluster, the bubble could slip freely along the curved FLAMS (Video S5, Supporting Information). Different from most of the bubble manipulation strategies,[10−12,14,32] our approach shows high performance complex 3-D motion.

Finally, the proof-of-concept "bubble mini-robot" (BMR) was demonstrated in precise control and high towing capacity for steering macroscopic objects. The experimental setup and related schematics are depicted in Figure 5a, in which a 15 μL bubble was employed to control the motion of a plastic fish (7 mg) on the air−water interface. The upper surface of BMR was in contact with the lower surface of the fish head so as to manipulate the plastic fish under the assistance of magnetic force and interfacial affinity. The reorientation of the plastic fish was achieved by dynamic rotation of the bubble. Figure 5b,c demonstrates how a BMR distributes the floating polymer spheres. The fish mouth, consisting of a pair of slender tweezers, was built for detaching and clamping the colored polymer sphere on the air−water interface. The sphere mass
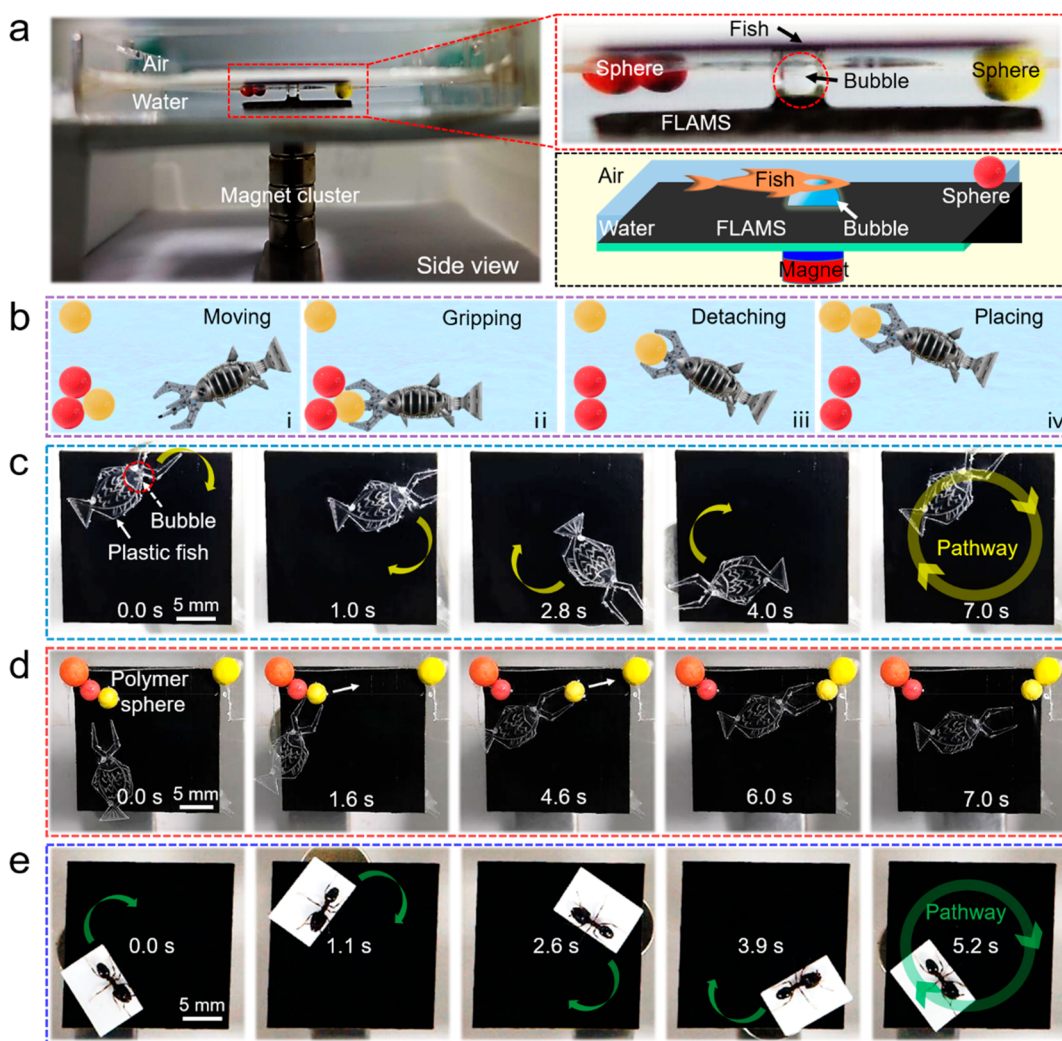
Figure 5. Precise control and high towing capacity utilizing "bubble mini-robot" (BMR). (a) Side view of experimental setup is shown. (b) Schematic of a BMR-actuated manipulator (plastic fish) is shown. (c) The manipulator completes a circular motion within 7 s, showing good maneuverability. (d) The left yellow sphere is detached by the fish mouth and then transported to the right corner. Consequently, the colored spheres are regrouped according to their colors. (e) A carpenter ant is steered by BMR on the air−water interface.

was measured to be 0.56 mg, and the bubble mass was calculated as ∼0.02 mg by ignoring the volumetric change arriving from the water pressure. The plastic fish completed a circular motion within 7 s, showing good maneuverability (Video S6, Supporting Information). In Figure 5d, the left yellow sphere was precisely detached from the sphere cluster by the fish mouth and clamped steady to the right corner within 7 s (Video S7, Supporting Information). Going further, our BMR can also effectively perform organism delivery. Figure 5e demonstrates the manipulation of a carpenter ant on a plastic sheet (also see Figure S10 and Video S8, Supporting Information). Additional demonstrations such as manipulating green leaf (10 mg) and pink petal (3 mg) are also performed (Figure S11 and Video S9, Supporting Information). These pioneering explorations reveal that a FLAMS-attached bubble exhibits high towing capacity of precisely steering a much heavier object (>500 own mass) on the air−water interface, which is inaccessible for previous bubble manipulation strategies.

To conclude, we have demonstrated high performance bubble manipulation on the FLAMS: ultrafast horizontal transport, complex actions toward arbitrary direction (i.e.,

antibuoyancy motion, "freestyle writing", bubble programmable coalescence, and 3-D controllable motion) and high towing capacity of steering macroscopic objects on the air−water interface. Particularly, typical bubble can be accelerated at >150 mm/s^2 and transported at an ultrafast velocity over 25 mm/s on horizontal platform. On this basis, the high towing capacity of the bubble was unfolded by steering macroscopic object (>500 own mass) on the air−water interface. This strategy exhibits not only excellent bubble manipulation performance, but also the capability of matter delivery, which are otherwise inaccessible for conventional buoyancy- or wetting/Laplace-gradient-assisted approaches suffering from unidirectional transport on tailor-made platforms. Moreover, the customizability of manipulation performance is embodied in adjusting diverse experimental parameters including laser-ablation conditions, magnetic forces, and ferrofluid properties (e.g., the geography of substrate, the concentration of magnetic particles or the type and viscosity of the carrier fluid), which would further broaden its practical applicability. This work provides new insights for the smart control of underwater bubbles and the development of gas-related microfluidic devices, water treatment, and electrochemistry.

METHODS

Synthesis of the Ferrofluid. Iron oxide nanocrystals were synthesized with the coprecipitation method. $FeCl_3 \cdot 6H_2O$ (5.4 g, 20 mmol) was added to a 200 mL water solution containing $FeCl_2 \cdot 4H_2O$ (2.0 g, 10 mmol) and then stirred for 30 min. $NH_3 \cdot 4H_2O$ (25 wt %, 7 mL) was added dropwise to the mixture under vigorous stirring, resulting in the formation of Fe_3O_4 nanocrystals in weak alkaline solution. After stirring for 3 h, the resulting precipitate was isolated from the mixture with a strong magnet, washed with deionized water three times. Oleic acid (1.22 g, 4.3 mmol) was added dropwise to Fe_3O_4/ water suspension at 80 °C under nitrogen protection and continuous stirring for 30 min. Finally, the surface-modified Fe_3O_4 nanocrystals were uniformly dispersed in normal octane (3.2 mL, 20 mmol) and ready for use. Here octane was chosen to satisfy the basic criterion that the carrier fluid for iron oxide nanoparticles should be aerophilic with low viscosity and immiscible with ambient water.

Preparation of the FLAMS. Mechanically polished $Ni_{55.7}Ti_{44.3}$ sheets (20 × 20 mm², thickness 2 mm, purity 99.8%), labeled Ni−Ti alloy, were cleaned ultrasonically in acetone and deionized water, respectively. The cleaned sample was irradiated by vertically crossed line-by-line femtosecond laser scanning (central wavelength of 800 nm, 1 kHz train of 104 fs) from a femtosecond laser system (Coherent, Legend Elite-1K-HE, USA). The laser beam was focused onto the sample surface and scanned along the $x−y$ coordinate direction through a galvanometric scanning system (ScanLab, Germany). The scanning spacing between two adjacent lines was 20 μm in both x and y coordinates direction. The measured mean power of the laser beam was 240 mW on a 20 μm spot. The scanning speed was set to 2 mm/s. The total laser-ablation time is approximately about 66 min for typical ferrofluid-infused area of 10 × 10 mm². The microstructured surfaces were treated into superhydrophobic and then infused with ferrofluid under water.

Measurement of the Ferrofluid Thickness. The microstructured sample was put on the microscope worktable. The first numerical value was recorded when the microscope focused on the bottom grooves of the microstructures. After that, a certain amount of ferrofluid was in situ infused into the microstructured surface of the sample. Then the second value was recorded when the microscope focused on the upper surface of the ferrofluid. Finally, the ferrofluid thickness was figured out according to the numerical-value difference and the microscope resolution (2 μm).

Characterization. The contact angles of the bubbles were measured on the as-prepared FLAMS with a contact-angle system (Innuo CA100C, China) by a sessile drop method. Surface morphologies of the laser-textured Ni−Ti alloy sheet were observed by a secondary electron scanning electron microscope (Zeiss EVO18) with an accelerating voltage at 10 kV.

ASSOCIATED CONTENT

Supporting Information

The Supporting Information is available free of charge at https://pubs.acs.org/doi/10.1021/acs.nanolett.0c02091.

Bubble motion response under different driving velocity (MP4)

"Free-style writing" of the bubbles (MP4)

Bubble programmable coalescence (MP4)

Antibuoyancy motion of the bubbles (MP4)

Controllable 3-D motion of the bubbles (MP4)

Bubble mini-robot powered plastic fish (MP4)

Manipulating polymer spheres by bubble mini-robot (MP4)

Manipulating carpenter ant by bubble mini-robot (MP4)

Manipulating plants by bubble mini-robot (MP4)

Schematic of the optical systems and pathways, water and bubble contact angle measurement, synthesis of the ferrofluid, SEM structure images, maximum bubble load on the FLAMS, highspeed imaging system, schematic of the bubble driving system, images of meniscus deformation, comparison of bubble motion efficiency with various marine lives, proof-of-concept BMR, images of matter transport of a leaf and petal (PDF)

AUTHOR INFORMATION

Corresponding Authors

Jiawen Li − *CAS Key Laboratory of Mechanical Behavior and Design of Materials, Key Laboratory of Precision Scientific Instrumentation of Anhui Higher Education Institutes, Department of Precision Machinery and Precision Instrumentation, University of Science and Technology of China, Hefei 230026, China;* orcid.org/0000-0003-3950-6212; Email: jwl@ustc.edu.cn

Yanlei Hu − *CAS Key Laboratory of Mechanical Behavior and Design of Materials, Key Laboratory of Precision Scientific Instrumentation of Anhui Higher Education Institutes, Department of Precision Machinery and Precision Instrumentation, University of Science and Technology of China, Hefei 230026, China;* orcid.org/0000-0003-1964-0043; Email: huyl@ustc.edu.cn

Dong Wu − *CAS Key Laboratory of Mechanical Behavior and Design of Materials, Key Laboratory of Precision Scientific Instrumentation of Anhui Higher Education Institutes, Department of Precision Machinery and Precision Instrumentation, University of Science and Technology of China, Hefei 230026, China;* orcid.org/0000-0003-0623-1515; Email: dongwu@ustc.edu.cn

Authors

Suwan Zhu − *CAS Key Laboratory of Mechanical Behavior and Design of Materials, Key Laboratory of Precision Scientific Instrumentation of Anhui Higher Education Institutes, Department of Precision Machinery and Precision Instrumentation, University of Science and Technology of China, Hefei 230026, China*

Yucheng Bian − *School of Microelectronics, University of Science and Technology of China, Hefei 230026, China*

Tao Wu − *Department of Modern Mechanics, University of Science and Technology of China, Hefei 230026, China;* orcid.org/0000-0002-0291-6595

Chao Chen − *CAS Key Laboratory of Mechanical Behavior and Design of Materials, Key Laboratory of Precision Scientific Instrumentation of Anhui Higher Education Institutes, Department of Precision Machinery and Precision Instrumentation, University of Science and Technology of China, Hefei 230026, China*

Yunlong Jiao − *CAS Key Laboratory of Mechanical Behavior and Design of Materials, Key Laboratory of Precision Scientific Instrumentation of Anhui Higher Education Institutes, Department of Precision Machinery and Precision*

Instrumentation, University of Science and Technology of China, Hefei 230026, China; ◯ orcid.org/0000-0001-7718-7342

Zhiwu Jiang − *Department of Modern Mechanics, University of Science and Technology of China, Hefei 230026, China*

Zhouchen Huang − *CAS Key Laboratory of Mechanical Behavior and Design of Materials, Key Laboratory of Precision Scientific Instrumentation of Anhui Higher Education Institutes, Department of Precision Machinery and Precision Instrumentation, University of Science and Technology of China, Hefei 230026, China*

Erqiang Li − *Department of Modern Mechanics, University of Science and Technology of China, Hefei 230026, China*

Jiaru Chu − *CAS Key Laboratory of Mechanical Behavior and Design of Materials, Key Laboratory of Precision Scientific Instrumentation of Anhui Higher Education Institutes, Department of Precision Machinery and Precision Instrumentation, University of Science and Technology of China, Hefei 230026, China;* ◯ orcid.org/0000-0001-6472-8103

Lei Jiang − *Key Laboratory of Bio-inspired Materials and Interfacial Science, Technical Institute of Physics and Chemistry, Chinese Academy of Sciences, Beijing 100190, China;* ◯ orcid.org/0000-0003-4579-728X

Complete contact information is available at:
https://pubs.acs.org/10.1021/acs.nanolett.0c02091

Author Contributions

S.Z., D.W., Y.H., and L.J. conceived and designed the experiments. S.Z., Y.B., T.W., Z.H., Y.J., and C.C. performed the experiments. S.Z., T.W., and Z.J. analyzed the data. S.Z. and Y.B. wrote the manuscript with assistance from all authors. D.W., E.L., J.L., Y.H., and J.C. contributed the materials and experimental instruments. S.Z. and Y.B. contributed equally to this work.

Notes

The authors declare no competing financial interest.

■ REFERENCES

(1) Odegaard, H. The Use of Dissolved Air Flotation in Municipal Wastewater Treatment. *Water Sci. Technol.* **2001**, *43*, 75−81.

(2) Sarkar, M. S. K. A.; Donne, S. W.; Evans, G. M. Hydrogen Bubble Flotation of Silica. *Adv. Powder Technol.* **2010**, *21*, 412−418.

(3) Kolb, G.; Hessel, V. Micro-Structured Reactors for Gas Phase Reactions. *Chem. Eng. J.* **2004**, *98*, 1−38.

(4) Li, Y. J.; Zhang, H. C.; Xu, T. H.; Lu, Z. Y.; Wu, X. H.; Wan, P. B.; Sun, X. M.; Jiang, L. Under-Water Superaerophobic Pine-Shaped Pt Nanoarray Electrode for Ultrahigh-Performance Hydrogen Evolution. *Adv. Funct. Mater.* **2015**, *25*, 1737−1744.

(5) Wiley, D.; Ware, C.; Bocconcelli, A.; Cholewiak, D.; Friedlaender, A.; Thompson, M.; Weinrich, M. Underwater Components of Humpback Whale Bubble-Net Feeding Behavior. *Behaviour* **2011**, *148*, 575−602.

(6) Pioro, I. L.; Rohsenow, W.; Doerffer, S. S. Nucleate Pool-Boiling Heat Transfer. II: Assessment of Prediction Methods. *Int. J. Heat Mass Transfer* **2004**, *47*, 5045−5057.

(7) Rao, G. V.; Balakrishnan, A. R. Heat Transfer in Nucleate Pool Boiling of Multicomponent Mixtures. *Exp. Therm. Fluid Sci.* **2004**, *29*, 87−103.

(8) Taboas, F.; Valles, M.; Bourouis, M.; Coronas, A. Pool Boiling of Ammonia/Water and Its Pure Components: Comparison of Experimental Data in the Literature with the Predictions of Standard Correlations. *Int. J. Refrig.* **2007**, *30*, 778−788.

(9) Spindler, K. Overview and Discussion on Pool Boiling Heat Transfer Data and Correlations of Ammonia. *Int. J. Refrig.* **2010**, *33*, 1292−1306.

(10) Jiao, Y. L.; Lv, X. D.; Zhang, Y. Y.; Li, C. Z.; Li, J. W.; Wu, H.; Xiao, Y.; Wu, S. Z.; Hu, Y. L.; Wu, D.; Chu, J. R. Pitcher Plant-Bioinspired Bubble Slippery Surface Fabricated by Femtosecond Laser for Buoyancy-Driven Gas Self-Transport and Efficient Capture. *Nanoscale* **2019**, *11*, 1370−1378.

(11) Yu, C. M.; Zhu, X. B.; Li, K.; Cao, M. Y.; Jiang, L. Manipulating Bubbles in Aqueous Environment via a Lubricant-Infused Slippery Surface. *Adv. Funct. Mater.* **2017**, *27*, 1701605.

(12) Tang, X.; Xiong, H. R.; Kong, T. T.; Tian, Y.; Li, W. D.; Wang, L. Q. Bioinspired Nanostructured Surfaces for On-Demand Bubble Transportation. *ACS Appl. Mater. Interfaces* **2018**, *10*, 3029−3038.

(13) Xiao, X.; Zhang, C. H.; Ma, H. Y.; Zhang, Y. H.; Liu, G. L.; Cao, M. Y.; Yu, C. M.; Jiang, L. Bioinspired Slippery Cone for Controllable Manipulation of Gas Bubbles in Low-Surface-Tension Environment. *ACS Nano* **2019**, *13*, 4083−4090.

(14) Zhang, C. H.; Zhang, B.; Ma, H. Y.; Li, Z.; Xiao, X.; Zhang, Y. H.; Cui, X. Y.; Yu, C. M.; Cao, M. Y.; Jiang, L. Bioinspired Pressure-Tolerant Asymmetric Slippery Surface for Continuous Self-Transport of Gas Bubbles in Aqueous Environment. *ACS Nano* **2018**, *12*, 2048−2055.

(15) Yu, C. M.; Cao, M. Y.; Dong, Z. C.; Wang, J. M.; Li, K.; Jiang, L. Spontaneous and Directional Transportation of Gas Bubbles on Superhydrophobic Cones. *Adv. Funct. Mater.* **2016**, *26*, 3236−3243.

(16) Yu, C. M.; Zhu, X. B.; Cao, M. Y.; Yu, C. L.; Li, K.; Jiang, L. Superhydrophobic Helix: Controllable and Directional Bubble Transport in an Aqueous Environment. *J. Mater. Chem. A* **2016**, *4*, 16865−16870.

(17) Shin, J. H.; Seo, J.; Hong, J.; Chung, S. K. Hybrid Optothermal and Acoustic Manipulations of Microbubbles for Precise and On-Demand Handling of Micro-Objects. *Sens. Actuators, B* **2017**, *246*, 415−420.

(18) Zhang, C. H.; Cao, M. Y.; Ma, H. Y.; Yu, C. L.; Li, K.; Yu, C. M.; Jiang, L. Morphology-Control Strategy of the Superhydrophobic Poly (Methyl Methacrylate) Surface for Efficient Bubble Adhesion and Wastewater Remediation. *Adv. Funct. Mater.* **2017**, *27*, 1702020.

(19) Wong, T. S.; Kang, S. H.; Tang, S. K. Y.; Smythe, E. J.; Hatton, B. D.; Grinthal, A.; Aizenberg, J. Bioinspired Self-Repairing Slippery Surfaces with Pressure-Stable Omniphobicity. *Nature* **2011**, *477*, 443−447.

(20) Xiang, T. F.; Zheng, S. L.; Zhang, M.; Sadig, H. R.; Li, C. Bioinspired Slippery Zinc Phosphate Coating for Sustainable Corrosion Protection. *ACS Sustainable Chem. Eng.* **2018**, *6*, 10960−10968.

(21) Kreder, M. J.; Alvarenga, J.; Kim, P.; Aizenberg, J. Design of Anti-Icing Surfaces: Smooth, Textured or Slippery? *Nat. Rev. Mater.* **2016**, *1*, 15003.

(22) Amini, S.; Kolle, S.; Petrone, L.; Ahanotu, O.; Sunny, S.; Sutanto, C. N.; Hoon, S.; Cohen, L.; Weaver, J. C.; Aizenberg, J. Preventing Mussel Adhesion Using Lubricant-Infused Materials. *Science* **2017**, *357*, 668−673.

(23) Wang, W. D.; Timonen, J. V. I.; Carlson, A.; Drotlef, D. M.; Zhang, C. T.; Kolle, S.; Grinthal, A.; Wong, T. S.; Hatton, B.; Kang, S.

H.; Kennedy, S.; Chi, J.; Blough, R. T.; Sitti, M.; Mahadevan, L.; Aizenberg, J. Multifunctional Ferrofluid-Infused Surfaces with Reconfigurable Multiscale Topography. *Nature* **2018**, *559*, 77−82.

(24) Khalil, K. S.; Mahmoudi, S. R.; Abu-dheir, N.; Varanasi, K. K. Active Surfaces: Ferrofluid-Impregnated Surfaces for Active Manipulation of Droplets. *Appl. Phys. Lett.* **2014**, *105*, No. 041604.

(25) Massart, R. Preparation of Aqueous Magnetic Liquids in Alkaline and Acidic Media. *IEEE Trans. Magn.* **1981**, *17*, 1247−1248.

(26) Gennes, P. G.; Brochard-Wyart, F.; Quéré, D. *Capillarity and Wetting Phenomena: Drops, Bubbles, Pearls, Waves*; Springer: New York, 2004.

(27) Neeson, M. J.; Tabor, R. F.; Grieser, F.; Dagastine, R. R.; Chan, D. Y. C. Compound Sessile Drops. *Soft Matter* **2012**, *8*, 11042−11050.

(28) Li, E. Q.; Al-Otaibi, S. A.; Vakarelski, I. U.; Thoroddsen, S. T. Satellite Formation During Bubble Transition through an Interface between Immiscible Liquids. *J. Fluid Mech.* **2014**, *744*, R1.

(29) Kavehpour, H. P. Coalescence of Drops. *Annu. Rev. Fluid Mech.* **2015**, *47*, 245−268.

(30) Clanet, C.; Quéré, D. Onset of Menisci. *J. Fluid Mech.* **2002**, *460*, 131−149.

(31) Chen, C.; Huang, Z. C.; Shi, L. A.; Jiao, Y. L.; Zhu, S. W.; Li, J. W.; Hu, Y. L.; Chu, J. R.; Wu, D.; Jiang, L. Remote Photothermal Actuation of Underwater Bubble toward Arbitrary Direction on Planar Slippery Fe_3O_4-Doped Surfaces. *Adv. Funct. Mater.* **2019**, *29*, 1904766.

(32) Guo, P.; Wang, Z. B.; Heng, L. P.; Zhang, Y. Q.; Wang, X.; Jiang, L. Magnetocontrollable Droplet and Bubble Manipulation on a Stable Amphibious Slippery Gel Surface. *Adv. Funct. Mater.* **2019**, *29*, 1808717.

(33) Walters, V.; Fierstine, H. L. Measurements of Swimming Speeds of Yellowfin Tuna and Wahoo. *Nature* **1964**, *202*, 208−209.

(34) Furmidge, C. G. L. Studies at phase interfaces. I. The Sliding of Liquid Drops on Solid Surfaces and a Theory for Spray Retention. *J. Colloid Sci.* **1962**, *17*, 309−324.

(35) Loudet, J. C.; Hanusse, P.; Poulin, P. Stokes Drag on a Sphere in a Nematic Liquid Crystal. *Science* **2004**, *306*, 1525.